A&A 514, A5 (2010)
DOI: 10.1051/0004-6361/200913466

Astronomy & Astrophysics
Special feature

Science with AKARI

Polycyclic aromatic hydrocarbon (PAH) luminous galaxies at $z \sim 1$

T. Takagi[1], Y. Ohyama[2], T. Goto[3,4], H. Matsuhara[1], S. Oyabu[1], T. Wada[1], C. P. Pearson[5], H. M. Lee[6], M. Im[6], M. G. Lee[6], H. Shim[6], H. Hanami[7], T. Ishigaki[8], K. Imai[9], G. J. White[5,10], S. Serjeant[10], and M. Malkan[11]

[1] Institute of Space and Astronautical Science, Japan Aerospace Exploration Agency, Sagamihara, Kanagawa 229-8510, Japan
e-mail: takagi@ir.isas.jaxa.jp
[2] Academia Sinica, Institute of Astronomy and Astrophysics, Taiwan
[3] Institute for Astronomy, University of Hawaii, 2680 Woodlawn Drive, Honolulu, HI, 96822, USA
[4] National Astronomical Observatory, 2-21-1 Osawa, Mitaka, Tokyo, 181-8588, Japan
[5] Rutherford Appleton Laboratory, Chilton, Didcot, Oxfordshire, OX11 0QX, UK
[6] Department of Physics and Astronomy, FPRD, Seoul National University, Shilim-Dong, Kwanak-Gu, Seoul 151-742, Korea
[7] Physics Section, Faculty of Humanities and Social Sciences, Iwate University, Morioka 020-8550, Japan
[8] Asahikawa National College of Technology, Asahikawa, Hokkaido 071-8124, Japan
[9] TOME R&D Inc. Kawasaki, Kanagawa 213-0012, Japan
[10] Astrophysics Group, Department of Physics, The Open University, Milton Keynes, MK7 6AA, UK
[11] Department of Physics and Astronomy, UCLA, Los Angeles, CA, USA

Received 14 October 2009 / Accepted 17 February 2010

ABSTRACT

Aims. The NEP-deep survey, an extragalactic AKARI survey towards the north ecliptic pole (NEP), provides a comprehensive wavelength coverage from 2 to 24 μm using all 9 photometric bands of the infrared camera (IRC). It allows us to photometrically identify galaxies whose mid-IR emission is clearly dominated by PAHs.
Methods. We propose a single-colour selection method to identify such galaxies, using two mid-IR flux ratios at 11-to-7 μm and 15-to-9 μm (PAH-to-continuum flux ratio in the rest frame), which are useful for identifying starburst galaxies at $z \sim 0.5$ and 1, respectively. We perform a fitting of the spectral energy distributions (SEDs) from optical to mid-IR wavelengths, using an evolutionary starburst model with a proper treatment of radiative transfer (SBURT), in order to investigate their nature.
Results. The SBURT model reproduces observed optical-to-mid-IR SEDs of more than a half of the PAH-selected galaxies. Based on the 8 μm luminosity, we find ultra luminous infrared galaxies (ULIRGs) among PAH-selected galaxies. Their PAH luminosity is higher than local ULIRGs with a similar luminosity, and the PAH-to-total IR luminosity ratio is consistent with that of less luminous starburst galaxies. They are a unique galaxy population at high redshifts, and we call these PAH-selected ULIRGs "PAH-luminous" galaxies. Although they are not as massive as submillimetre galaxies at $z \sim 2$, they have the stellar mass of $>3 \times 10^{10}\ M_{\odot}$ and therefore are moderately massive.

Key words. galaxies: starburst – infrared: galaxies – galaxies: active – galaxies : evolution

1. Introduction

In recent studies of galaxy formation and evolution, the most massive and luminous galaxies have played a leading role. Most luminous galaxies, such as submillimetre galaxies and ultraluminous infrared galaxies (ULIRGs[1]) at high redshifts are now believed to be the progenitors of massive spheroids and to highlight the early formation of massive galaxies (e.g. Smail et al. 2004; Chapman et al. 2005; Tacconi et al. 2008). This supports the scenario of anti-hierarchical or "down-sizing" galaxy formation (e.g. Heavens et al. 2004; Cimatti et al. 2006).

Mid-infrared (IR) surveys are a powerful tool for studying the most luminous galaxies at high redshifts by providing the infrared luminosity function and the star formation rate in a large cosmic volume as a function of redshift (e.g. Pérez-González et al. 2005; Le Floc'h et al. 2005; Babbedge et al. 2006; Caputi et al. 2007; Goto et al. 2010). However, this work can suffer uncertainty from the k-correction, which requires knowing the appropriate mid-IR spectral energy distribution (SED). In fact, sensitive IRS observations with the *Spitzer* space telescope reveal that the mid-IR spectra of submillimetre galaxies resembles that of over 2 orders of magnitude less luminous starburst galaxies (Valiante et al. 2007; Pope et al. 2008; Farrah et al. 2008), which have prominent emission features of polycyclic aromatic hydrocarbons (PAHs). This raises questions about the nature of most luminous galaxies and how they differ systematically from low-z to high-z.

Multi-wavelength mid-IR surveys with AKARI provide a unique measure of the mid-IR properties of infrared galaxies at high redshifts with a statistically valid sample. Takagi et al. (2007a) demonstrate that AKARI/IRC all-band photometry is capable of identifying the approximate spectral shape of the PAH emission, specifically the steep rise in flux at the blue side of the PAH 6.2 μm feature. Such a steep flux rise can only be accounted for by PAH emission. Using this fact, we propose a new photometric selection method for galaxies whose mid-IR emission is dominated by PAH emission. This is possible if photometric observations are comprehensive enough to trace the PAH emission feature in the SED, as in the

[1] Galaxies with a total infrared (8–1000 μm) luminosity of $10^{12-13}\ L_{\odot}$.

AKARI/IRC all-band photometric survey. We call galaxies selected in this method PAH-selected galaxies.

In this paper, we utilise the multi-wavelength mid-IR coverage of the NEP-deep survey with AKARI to identify galaxies with strong PAH emission. Sections 2 and 3 describe the data and sample selection, respectively. Our SED-fitting method using the optical to mid-IR wavelength range and its results are presented in Sect. 4. We discuss the properties of PAH-selected galaxies in Sect. 5 and summarise the results in Sect. 6. Throughout this paper, a flat cosmology with $H_0 = 70\,\mathrm{km\,s^{-1}\,Mpc^{-1}}$ and $\Omega_\Lambda = 0.7$ is used. All magnitudes are given in the AB system, unless otherwise stated.

2. Data

Here we use the multi-wavelength data set of the AKARI NEP-deep survey, described in detail in Wada et al. (2008). The NEP-deep survey covers a circular area of 0.38 deg^2, centred at $\alpha = 17^{\mathrm{h}}56^{\mathrm{m}}01^{\mathrm{s}}$ and $\delta = 66°33'48.4''$ (J2000.0), with all nine IRC bands, i.e. 2.4, 3.2, 4.1, 7.0, 9.0, 11, 15, 18, and 24 μm ($N2$, $N3$, $N4$, $S7$, $S9W$, $S11$, $L15$, $L18W$, and $L24$ in conventional band names, respectively). The 5σ sensitivities in these bands are 9.6[1], 7.5[1], 5.4[2], 49, 58, 71, 117, 121, and 275 μJy from $N2$ to $L24$, respectively (Wada et al. 2008). Deep optical ($BVRi'z'$ and $NB711$) images with the Subaru/Suprime-cam (S-cam), reaching a limiting magnitude of $B = 28$ and $z' = 26$ AB mag, are available for a part of the NEP-deep field with an area of $27' \times 34'$, i.e. one field-of-view of S-cam. We also have ground-based near-IR (JK_s) images with KPNO-2.1 m/FLAMINGOS for the S-cam field (Imai et al. 2007), reaching a Vega magnitude of $K_\mathrm{s} = 19.5$. The ground-based near-IR images have higher spatial resolution (*FWHM* of 1.08″) than that of IRC, and are therefore quite useful for resolving source confusion in IRC images. In this paper, we concentrate on sources in the S-cam field.

We performed an optical spectroscopic survey of 242 mid-IR sources with $R \lesssim 24$ mag in the S-cam field using Keck/DEIMOS (Takagi et al., in prep.). Here we use the spectroscopic redshifts for calibrating photometric redshifts. The optical emission line diagnostics of mid-IR sources will be given elsewhere.

3. Sample selection

3.1. All-band-detected sources

To evaluate and to maximize the new diagnostic capabilities becoming available from the NEP-deep survey, we have constructed a source catalogue of objects, detected in all nine IRC bands (hereafter all-band-detected sources). We combined the $S7, S9W, S11$-band images for source detection and used SExtractor (Bertin & Arnouts 1996) to make an initial catalogue. We then followed Takagi et al. (2007a) for photometry with IRC images, in which the aperture photometry with 2 pixel and 3 pixel radii are used for near-IR ($N2, N3, N4$) and mid-IR images ($S7, S9W, S11, L15, L18W, L24$), respectively. Appropriate aperture corrections were then applied. We also followed Takagi et al. (2007a) for band merging. Starting from the centroid position of $S11$ sources, we searched for the centroid in the other images. If the angular distance between centroids is less than 3″, the objects are considered to be the same (see Wada et al. 2008).

[2] Corrected from the values in Wada et al. (2008), in which the adopted conversion factors for $N2$, $N3$, and $N4$ bands are not correct. The correct sensitivity is better by a factor of 1.47.

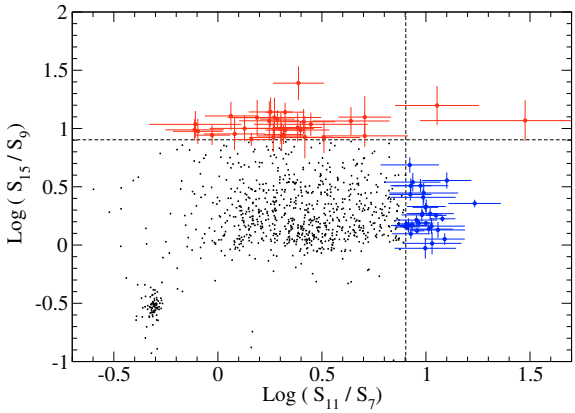

Fig. 1. A colour−colour plot of all-band-detected sources with 15-to-9 μm and 11-to-7 μm flux ratios. Dashed lines indicate the colour cuts for selecting PAH-selected galaxies. Points with error bars indicate the PAH-selected galaxies.

Since we have not adopted a specific signal-to-noise ratio for the detection at all of the IRC bands other than $S11$, the resulting catalogue includes less significant detections (<3σ) in some cases. Nevertheless, we include these sources in our all-band-detected sample, since the less significant detections are rare, and the resulting SED is still well constrained.

There are 1100 all-band-detected sources in the entire NEP-deep field, and 630 in the S-cam field. We searched for optical identification using sky positions in the $N2$ band, where the astrometry is based on the Two Micron All Sky Survey (2MASS) and therefore most reliable. The resulting optical identifications were all visually inspected. We found that about 10% of sources have ambiguous optical identifications. Excluding these sources, we obtained 568 all-band-detected sources in the S-cam field with unambiguous optical identification, of which 113 have optical spectra with DEIMOS.

3.2. PAH-selected galaxies

At the mid-IR wavelength region, emission from galaxies is usually dominated by small and hot dust grains experiencing the temperature fluctuation. PAHs are believed to be the smallest of those, consisting of ∼100 carbon atoms grouped into ∼10 Å in dimensions and having emission bands. PAH emission features have sometimes been used as star formation indicators, which are prominent in starburst galaxies (Brandl et al. 2006), but weak or absent in AGNs (Weedman et al. 2005).

Using the very steep flux rise on the blue side of the 6.2 μm PAH feature, we attempted to identify galaxies whose mid-IR emission is dominated by PAHs, based on AKARI photometric observations. The steep flux rise due to PAH emission can be characterised by the flux ratio at the rest-frame wavelengths of approximately 7 to 4 μm. For galaxies at $z \sim 0.5$ and 1, we could use 11-to-7 μm flux ratio and 15-to-9 μm flux ratio, respectively, in order to identify galaxies with prominent PAH emission. For convenience, we hereafter use the term, the PAH-to-continuum flux ratio, for these flux ratios. Figure 1 shows a colour−colour plot of all-band-detected sources using these flux ratios. There are galaxies with the PAH-to-continuum flux ratio as high as 10 for both ratios. We hereafter call galaxies with the flux ratio of >8 as PAH-selected galaxies.

For star-forming galaxies, it is likely that the flux at the rest-frame 4 μm is dominated by the stellar continuum, while PAH 7.7 μm feature dominates the flux at the rest-frame 7 μm.

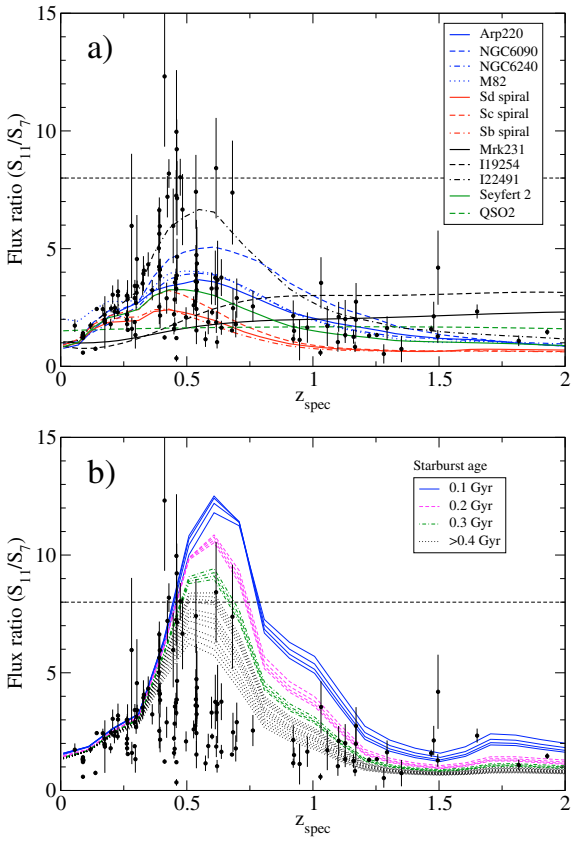

Fig. 2. 11-to-7 μm flux ratio as a function of redshift. Solid circles with error bars indicate the spectroscopic sample with $S_7, S_9, S_{11} > 30\,\mu$Jy, and $S_{15} > 100\,\mu$Jy. **a)** Flux ratio estimated from the SED template of Polletta et al. (2007). The names of galaxies in the template are given in the legend. **b)** Same as **a)**, but with the SBURT model with different starburst age and compactness of the starburst region (Θ = 1.4, 1.6, 1.8, 2.0), which controls the optical depth. The MW dust model is adopted. (*See the electronic edition of the Journal for a colour version of this figure.*)

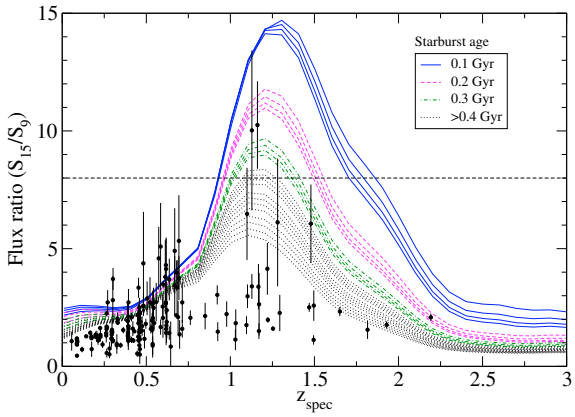

Fig. 3. Same as Fig. 2b), but for 15-to-9 μm flux ratio.

The PAH luminosity is believed to be a good tracer of total infrared luminosity of star-forming galaxies, hence the SFR (e.g. Genzel et al. 1998; Rigopoulou et al. 1999; Farrah et al. 2007). Thus, these flux ratios are roughly proportional to the mass-normalized SFRs, i.e. specific SFRs. We thus expect that PAH-selected galaxies are the best candidates for starburst galaxies.

In Fig. 2a, we show the 11-to-7 μm flux ratio as a function of redshift, using the SED template of various galaxy types – the SWIRE template library (Polletta et al. 2007). This template confirms that the 11-to-7 μm flux ratio has a peak at $z \sim 0.5$, although no SEDs in the template can reproduce the flux ratios greater than 8. The SWIRE template library has only a few SEDs of starburst-dominated galaxies. To explain the high flux ratio of PAH-selected galaxies, we may need more comprehensive SED templates of starburst galaxies.

For the comprehensive SED template of starburst galaxies, we adopted an evolutionary starburst SED model with radiative transfer (Takagi et al. 2003a, SBURT). This is an SED model for starburst regions, assumed to be spherical and to have a concentrated stellar distribution and homogeneous dust distribution. SBURT adopts a stellar population synthesis model of Kodama & Arimoto (1997) as input. The amount of dust is calculated, based on the chemical evolution assuming gas infall. The time scale of gas infall and of star formation is assumed to be 0.1 Gyr[3]. Thus, the SBURT model can be regarded as a population synthesis model with physically consistent treatment of dust extinction and re-emission. The optical depth of the system is controlled by the compactness (Θ) of the starburst region. In the SBURT model, there are three choices of the extinction curve, corresponding to the dust model for the Milky Way (MW), Large or Small Magellanic Clouds (LMC or SMC). The fraction of PAHs in dust is 5, 1, and 0.5% in the MW, LMC, and SMC dust models, respectively. Thus, models with the MW dust has the highest PAH-to-continuum flux ratio. See Takagi et al. (2003a,b) for more details of SBURT.

In Figs. 2b and 3, we show the 11-to-7 μm and 15-to-9 μm flux ratios estimated from the SBURT model, respectively. We found that the MW dust model is required, in order to reproduce high flux ratios of PAH-selected galaxies. According to the model, younger galaxies may have higher flux ratios, because the contribution from the stellar component to the 4 μm continuum is less for younger starbursts. The flux ratios over 8 are satisfied with the model younger than 0.4 Gyr. However, this is only one possible interpretation, since the dust model adopted has only three choices (MW, LMC, or SMC), and limited capability of reproducing large variations in mid-IR properties. Specifically, this model does not take the ionization status of PAHs into account, which significantly affects the optical constants of PAHs around 8 μm (e.g. Li & Draine 2001).

Among all-band-detected sources, we identified 56 (39) PAH-selected galaxies from the 11-to-7 μm (15-to-9 μm) flux ratio in the entire NEP-deep field, of which 38 (18) lie in the S-cam field with unambiguous optical identification. We include sources with less significant detection at the rest-frame 4 μm, if the 2.5σ upper limit is consistent with the selection criterion. In Table A.1, we tabulate the IRC photometry of PAH-selected galaxies.

4. Photometric redshifts and SED fits

4.1. Method

We fit the optical-to-MIR SEDs of all-band-detected sources with the SBURT model[4]. We use the model with the starburst

[3] The model SED of starbursts scales with the time scale of gas infall and star formation (Takagi et al. 2003a). Therefore, the starburst age from the SBURT model fitting should only be considered in the relative sense.

[4] The model grid is available at `http://www.ir.isas.jaxa.jp/~takagi/sedmodel/`.

age of 0.01−0.6 Gyr, which is long enough to represent the starburst phase. The SBURT model originally covers the wavelength range from UV to submillimetre. Takagi et al. (2007b) empirically added the radio component to reproduce the observed radio-IR correlation. This model does not include any emission from AGN. Thus, it is expected that the SBURT model underpredicts the mid-IR fluxes from AGN hosts, which usually have hot dust excess compared to pure starburst galaxies (Hunt et al. 1997).

We adopted the same SED fitting method as in Takagi et al. (2007a), using a standard χ^2 minimization technique. Takagi et al. (2007a) adopted relatively large minimum photometric errors, 20−30% depending on the band. Since the photometric calibration of IRC has been recently improved (Tanabé et al. 2008), we here set the minimum photometric errors to 15% for all IRC bands. As in Takagi et al. (2007a), we quadratically added an additional 20% error for data at the rest-frame UV wavelengths, <4000 Å, in order to account for the uncertainty of the extinction curve.

We applied the SBURT model to all-band-detected sources. By nature, all-band-detected sources are a heterogeneous sample, even including stars. Since we used a starburst SED template, SBURT, for this sample, it is important to distinguish starburst candidates from other types of sources. To do this, we used the goodness of SBURT fitting and reject sources with no acceptable SBURT model in further analyses. We reject the best-fitting SBURT model if the value of resulting χ^2 is so high that the corresponding probability is less than 1%.

4.2. Fitting results

4.2.1. All-band-detected sources

We performed SED-fitting for 568 all-band-detected sources using the SBURT model. We obtained good fits for ∼40% (211/568) of all-band-detected sources. On the other hand, using the SWIRE template library, instead of SBURT, we obtained good fits for only ∼10% (69/568) of the sources, although it covers a wide range of SED types. The SWIRE library only has a few SEDs of starbursts. We think that a wide variety of starburst SEDs, such as in the SBURT model, is needed to reproduce a good fraction of observed UV-mid-IR SEDs of IR-selected galaxies.

To show what kinds of sources are rejected in the SBURT fitting, we plot both accepted and rejected samples in a colour-colour plot of $N3-S7$ vs. $N2-N3$ in Fig. 4. Takagi et al. (2007a) used this colour−colour plot to differentiate AGNs from normal star-forming galaxies. AGNs identified with optical spectroscopy have red colours in both $N2-N3$ and $N3-S7$. The accepted fits avoid this AGN colour region, because the SBURT model does not have any AGN component. The accepted sample also avoids the clump of objects with blue colours at $N2-N3 \simeq 0.6$ and $N3-S7 \simeq -1.5$, which are stars. The rest of the rejected sample has similar $N2-N3$ and $N3-S7$ colours to those of the accepted sample. These include quiescent spiral galaxies, which have systematically redder optical-near-IR colours than any of the SBURT models. As we discuss in Sect. 5.1, limitations on the dust model may also cause rejection of the best-fitting model.

To derive any firm conclusions, photometric redshifts of the good-fit sample should be accurate enough. Figure 5 shows the comparison of photometric redshifts to spectroscopic redshifts. Defining a catastrophic error by $\frac{\Delta z}{(1+z)} > 0.2$, we find no catastrophic errors and $\sigma_{\frac{\Delta z}{(1+z)}} = 0.034$ for the good-fit sample, and 21/68 catastrophic errors for the bad-fit sample. Thus, the goodness of the SBURT fit is actually a good measure of the accuracy of photometric redshifts.

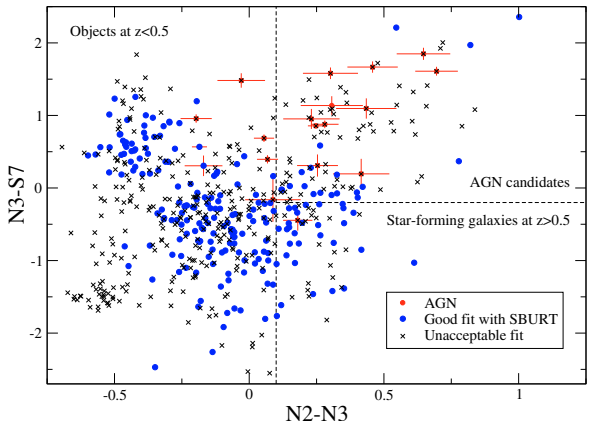

Fig. 4. Colour−colour plot with $N3-S7$ versus $N2-N3$. Solid circles and small crosses indicate the good and bad-fit samples, respectively. Solid circles with error bars represent optically identified AGN.

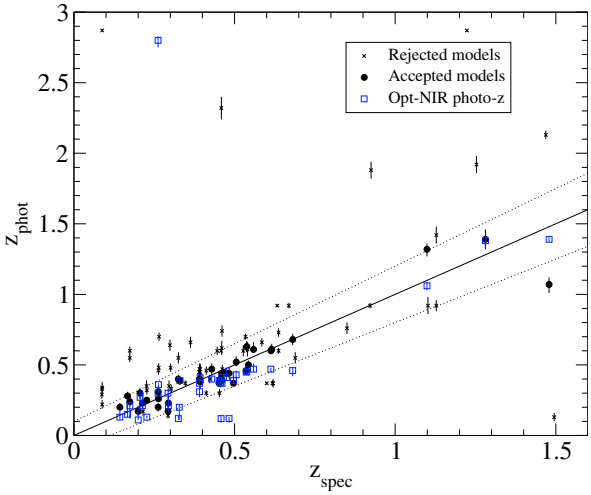

Fig. 5. Photometric versus spectroscopic redshifts. Solid circles indicate the redshifts of the good-fit sample, while small crosses are for the bad-fit sample. Dotted lines represent $\frac{\Delta z}{(1+z)} = \pm 0.1$. Squares indicate the photometric redshifts of the good-fit sample, based only on the ground-based optical-NIR photometry.

In Fig. 5, we also plot photometric redshifts derived only from ground-based optical-NIR ($BVRi'z'JK$) bands, using a widely-used photometric redshift code, Hyperz (Bolzonella et al. 2000). In Hyperz, we adopted a population synthesis model of Bruzual & Charlot (2003), which is distributed along with the code, and the extinction curve of starbursts (Calzetti et al. 2000) for dust reddening. In order to compare the photometric redshifts with AKARI bands to those without AKARI, we only show the good-fit sample (with SBURT fitting) in Fig. 5. We find one catastrophic error in ground-based photometric redshifts, while this galaxy has a reasonable photometric redshift with AKARI bands. Furthermore, ground-based photometric redshifts seem to have systematic errors; i.e., at $z \sim 0.5$, most of photometric redshifts are lower than the spectroscopic redshifts. These errors can be removed by using AKARI bands.

To check the statistical reliability of our photometric redshifts, we used a correlation between the NIR colour $N2-N3$ and redshift (Takagi et al. 2007a). With this test, we could detect systematic effects, if any, of using mid-IR fluxes for deriving

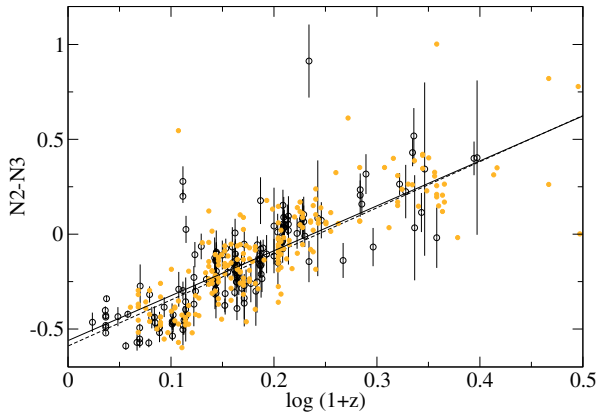

Fig. 6. Correlation between $N2-N3$ colour and redshift for both photometric and spectroscopic samples. Open circles with error bars indicate the spectroscopic sample. Solid circles represent the photometric sample. Solid and dashed lines are the regression line for photometric and spectroscopic sample, respectively.

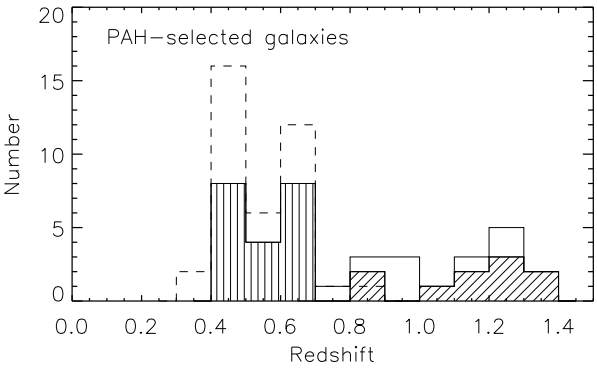

Fig. 7. Redshift distribution of PAH-selected galaxies. Vertically and diagonally shaded histograms represent 11-to-7 μm and 15-to-9 μm selected galaxies with good SED fits, respectively. Histograms with thin dashed and solid lines indicate the redshift distribution including the bad-fit sample. Spectroscopic redshifts are adopted if available.

photometric redshifts. In Fig. 6, we show the correlations for both spectroscopic and photometric samples. For the photometric sample, we obtain the correlation of $(N2 - N3) = (2.37 \pm 0.12)\log(1+z) - 0.56$, which is consistent with that of the spectroscopic sample, i.e. $(N2-N3) = (2.43 \pm 0.05)\log(1+z) - 0.59$. Therefore, we find no systematic errors in our photometric redshifts.

4.2.2. PAH-selected galaxies

We here show more details of SED fitting results specifically for PAH-selected galaxies. In Figs. A.1−A.4, we show the best-fitting (both accepted and rejected) SED models for PAH-selected galaxies at $z \sim 0.5$ and 1. We obtained acceptable SED fits for 22/38 and 10/18 of the PAH-selected galaxies at $z \sim 0.5$ and 1, respectively. Even though PAH-selected galaxies are starbursts, the SBURT model does not provide acceptable fits for 40% of PAH-selected galaxies, although the success rate of the fitting is better than for the whole sample. This topic is discussed in detail in the next section.

We show the redshift distributions of PAH-selected galaxies in Fig. 7. They are consistent with the expectation from the model templates, shown in Figs. 2 and 3. There are no systematic differences in photometric redshifts between the good- and bad-fit samples. This may indicate that the resulting large χ^2 does not come from an incorrect redshift. The total-IR luminosity from the SED model is indicated in each panel of Figs. A.1−A.4. The PAH-selected galaxies at $z \sim 1$ include ULIRGs. This type of ULIRGs can be found only at high redshifts (see Sect. 5.2).

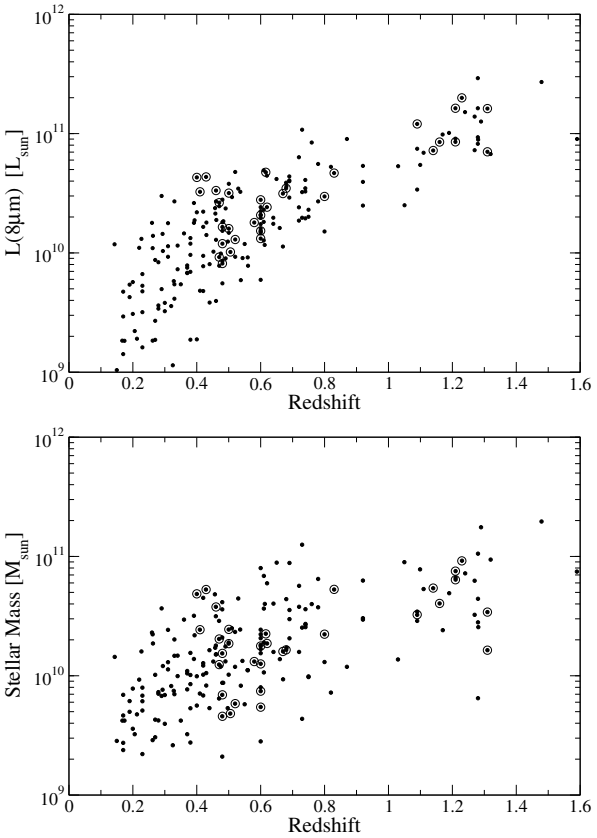

Fig. 8. 8 μm luminosity and stellar mass as a function of redshift. All-band-detected sources and PAH-selected galaxies are represented by small dots and open circles, respectively. We only show galaxies with good SED fits.

5. Discussion

5.1. Nature of PAH-selected galaxies

In Fig. 8, we show 8 μm luminosities and stellar masses of PAH-selected galaxies, along with those of all-band-detected sources. The 8 μm luminosity is derived from the observed flux in the IRC bands closest to the reset-frame 8 μm and the luminosity distance from photometric redshifts. Some of PAH-selected galaxies at $z \sim 1$ have $L_{8\,\mu m} > 10^{11}\ L_\odot$, which correspond to the luminosity of ULIRGs for a typical starburst SED (Weedman & Houck 2008).

Stellar masses are derived from the best-fitting SED model when it is accepted. The adopted initial mass function (IMF) is a top-heavy one with the power-law index of $x = 1.10$ (the Salpeter IMF has $x = 1.35$), and the lower and upper mass limits are 0.1 and 60 $M_\odot$ (see also Takagi et al. 2004). For the Salpeter IMF, stellar mass increases by a factor of 2. Stellar masses thus derived should be regarded as a lower limit, since the contribution from evolved stellar populations is not included. Most of PAH-selected galaxies at $z \sim 1$ have stellar masses of $>3 \times 10^{10}\ M_\odot$. Even some fraction of PAH-selected galaxies at $z \sim 0.5$ have similar stellar masses. What are descendants of

such massive PAH-selected, i.e. starburst galaxies? At redshift $z \sim 2$, massive starburst galaxies have been found mainly as sub-millimetre galaxies (SMGs; e.g. Borys et al. 2005), and they are good candidates for massive spheroids (Blain et al. 2004; Smail et al. 2004; Bouché et al. 2007; Tacconi et al. 2008). However, PAH-selected galaxies are not as massive as SMGs. Their luminosity is typically an order of magnitude less than that of SMGs, corresponding to luminous infrared galaxies (LIRGs[5]). Recent high-resolution images of LIRGs at $z \sim 1$ show that the majority of LIRGs have disk morphology (Elbaz et al. 2007; Melbourne et al. 2008), although the sample size is still small. Clearly, we need more comprehensive studies to identify what triggers the starburst activity of PAH-selected galaxies, in order to constrain their evolutionary path.

What is the main cause of a large PAH-to-continuum flux ratio? As shown in Figs. 2 and 3, the SBURT model predicts that galaxies with high PAH-to-continuum flux ratios are young starbursts with the starburst age of $\lesssim$0.4 Gyr. For the whole sample of PAH-selected galaxies with good SED fits, we derive the mean starburst age of 0.4 Gyr. In the SED fitting, the starburst age depends not only on the PAH-to-continuum flux ratio, but also on the optical colours (Takagi et al. 1999). The lack of very young starbursts in the sample may be accounted for by a selection effect, i.e. such young systems are hard to observe because of their short lifetimes.

Indeed, star-forming regions, i.e. young stellar systems in a galaxy, have a large PAH-to-continuum flux ratio, as shown in *Spitzer*/IRAC images of nearby galaxies in the literature. Wang et al. (2004) study the Antennae galaxies (NGC4038/4039) and show the map of the 8.0[6]-to-4.5 μm flux ratio, which is close to the PAH-to-continuum flux ratio in our definition. This flux ratio is quite high only in the overlap region of the two disks where the most of IR emission come from. They estimate that such active star-forming region comprise only ~10% of the total stellar mass of the entire system; i.e., the activity is localized rather than global. On the other hand, PAH-selected galaxies should have global star-forming activity, since the flux ratio for the entire system is high.

For a fair discussion, we should also pay attention to the case with *no* acceptable fits and clarify the cause of poor fits. In Fig. 9, we show the observed-to-model flux ratio as a function of rest-frame wavelength for PAH-selected galaxies at $0.4 < z < 0.5$. All of the rejected models, but one in Fig. 9, have a starburst age of 0.6 Gyr, that is the oldest and reddest model in the template. This means that the model-fitting fails for galaxies with relatively red optical colours, but with strong PAH emission (see also Ohyama et al., in prep.). Since the SBURT model is a rather simple model of starbursts, which only have a single starburst region and starburst stellar population, it is not surprising to find its limitation.

Figure 9 shows that a large discrepancy between observations and the model can be found in the 5−7 μm range with a sharp rising trend towards longer wavelength. We can see the same trend for the good-fit sample as well, although it is less significant. This indicates that the dust model adopted in the SBURT may need to be modified. One possibility is the ionization of PAHs. The optical constant of PAHs in the SBURT model is for neutral PAHs, which may not be true for all PAHs. Li & Draine (2001) suggest that ionized PAHs have systematically higher absorption cross section at 4−10 μm, compared to

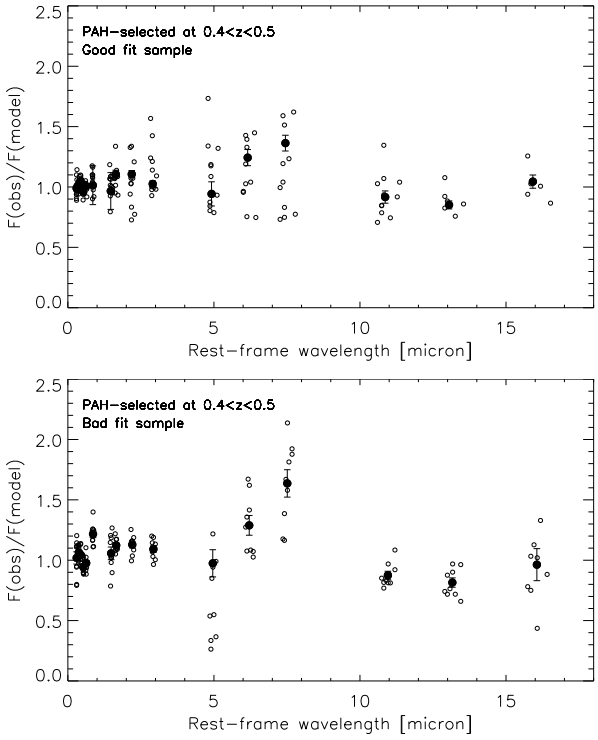

Fig. 9. Ratio of observed-to-model fluxes as a function of rest-frame wavelengths for PAH-selected galaxies at $0.4 < z < 0.5$. Open and solid circles indicate individual galaxies and the weighted average for each photometric band, assuming the mean redshift of 0.46 and 0.45 for good- and bad-fit samples, respectively.

neutral PAHs. If some fraction of PAHs are ionized, the discrepancies found in the SED fitting may be recovered.

Another possibility is that the stars dominating optical light are not the same as those responsible for strong PAH emission. As starbursts age, dust heating would mostly be dominated by newly formed stars in molecular clouds, while most of optical light come from stars having already exited from molecular clouds; i.e., older stars are less attenuated and dominate optical light, while younger stars embedded in dense molecular clouds dominate infrared light. Such age-dependent dust attenuation would be more effective in the later stage of starbursts. This may explain why we find larger discrepancy in optically red, probably old, starbursts.

The above two possibilities could be distinguished by the far-IR photometry. The former, the case of ionized PAHs, would change only mid-IR luminosity and does not affect the far-IR luminosity. If the latter (age-dependent attenuation) is the case, the current model would underestimate not only mid-IR luminosity but also far-IR luminosity. Thus, expected PAH-to-total-IR luminosity depends on the scenario. Sensitive far-IR photometry of red PAH-selected galaxies, e.g. with the *Herschel* Space Observatory, could have diagnostic power to identify the main cause of the discrepancy.

5.2. PAH-to-total IR luminosity relation

The PAH luminosity of local ULIRGs is less than the value expected from the correlation of PAH and total IR luminosity for less luminous starburst galaxies. In Fig. 10, we show this luminosity relation for galaxies at $z < 0.2$. The PAH luminosity is represented with the PAH 7.7 μm peak luminosity taken from Weedman & Houck (2008). The total infrared luminosity

[5] Galaxies with a total infrared (8−1000 μm) luminosity of 10^{11-12} $L_\odot$.
[6] Non-stellar emission, i.e. ~5% of stellar emission is subtracted from the total flux.

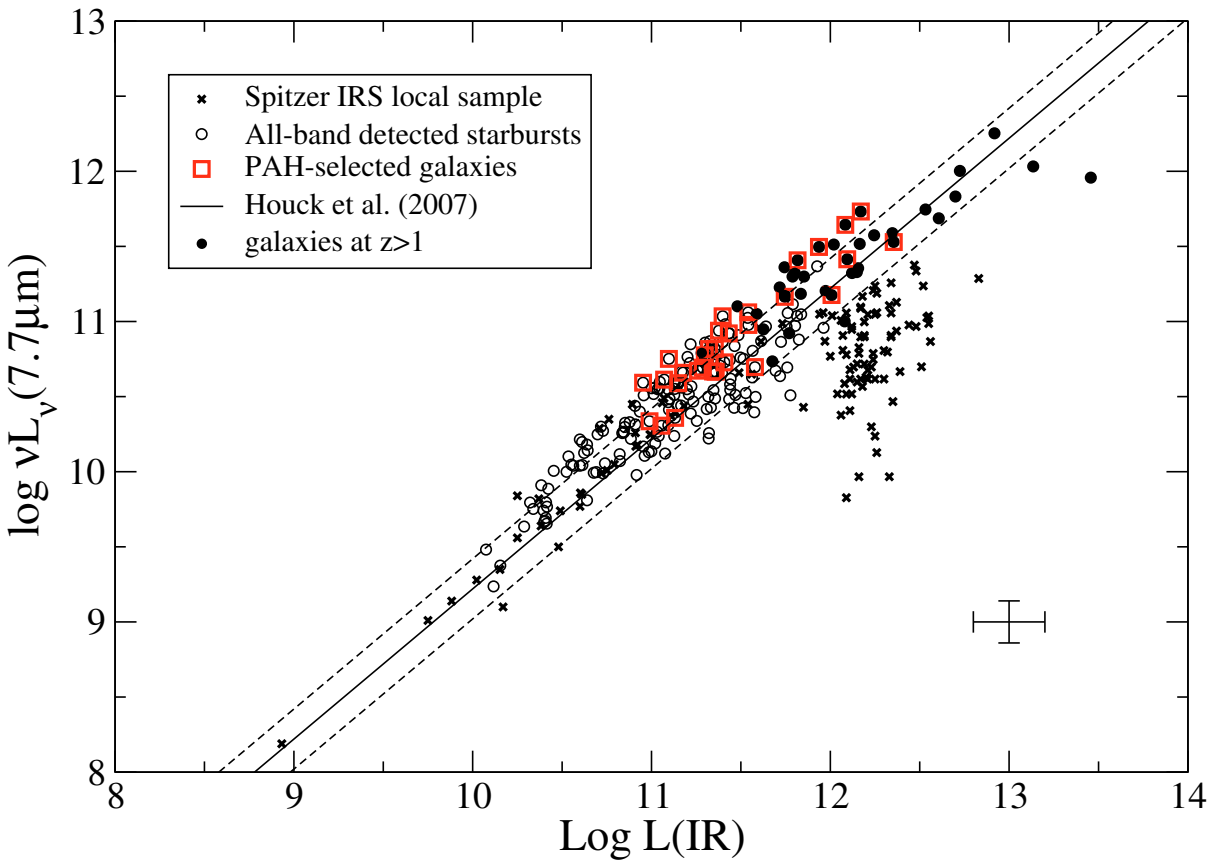

Fig. 10. 7.7 μm peak luminosity versus infrared luminosity. Solid and dashed lines represent the correlation between these luminosities found for less luminous starburst galaxies and its 1σ uncertainty (Houck et al. 2007). Legend describes symbols for local galaxies from *Spitzer* IRS sample from Weedman & Houck (2008), all-band-detected sources, and PAH-selected galaxies at both $z \sim 0.5$ and 1. Solid circles indicate galaxies with $z > 1$. Typical uncertainty of both luminosities is indicated in the bottom righthand corner.

is taken from the references in Weedman & Houck (2008), and converted to the cosmology adopted here. The 7.7 μm peak luminosity of ULIRGs is systematically below the correlation for local starbursts. A most plausible explanation of this systematic effect is an AGN contribution to the total IR luminosity. Imanishi et al. (2007) claim that 30−50% of optical non-Seyfert ULIRGs at $z < 0.15$ have dust-enshrouded AGN. Combined with optical Seyfert ULIRGs, their results indicate that ∼50% of ULIRGs at $z < 0.15$ harbour AGN (see also Genzel et al. 1998; Lutz et al. 1998). However, Fig. 10 shows that none of the $z < 0.2$ ULIRGs are consistent with the pure starburst case. This may indicate another explanation for the lower 7.7 μm luminosity of ULIRGs. If the starburst region is heavily obscured, the absorption of PAH emissions by silicate dust may not be negligible.

High-redshift ULIRGs may behave differently, owing to possible evolutionary effects. We investigated the PAH-to-total IR luminosity relation of the all-band-detected sources, including PAH-selected galaxies. The 7.7 μm peak luminosities are estimated from the IRC photometry by the following method. For a local starburst spectral template of Brandl et al. (2006), filter-convolved flux at the rest-frame 8 μm is approximately half of the 7.7 μm peak flux: 0.50 in the $L15$ filter at $z = 1$ and 0.42 for the $S11$ filter at $z = 0.5$, for example. Here we adopt 0.50 for the conversion factor, since $z \sim 1$ sources are our prime targets. This estimate would be accurate within a 30% uncertainty, as long as the 8 μm emission is dominated by starbursts. Intrinsic spectral variation at 5−8 μm is found to be small in starbursts (Nardini et al. 2008). The rest-frame 8 μm luminosities are estimated from the observed fluxes at the band closest to the rest-frame 8 μm and the luminosity distance derived from the redshift estimates. We have not done any interpolation or k-correction in this step, considering the uncertainty of the photometric redshift. The total IR luminosities are derived from the best-fitting SED model. Therefore, we only consider the good-fit sample. A well-known tight correlation between the global far-IR and radio emission allows us to check the reliability of estimated total-IR luminosity from the SED fitting. Among all-band-detected sources, we detected five galaxies in our 1.4 GHz observation with WSRT (White et al. 2010, in prep.), which covers a part of the NEP-deep field. By comparing the observed radio fluxes to those predicted from the best-fitting SBURT models based on the far-IR/radio correlation, we estimate that the derived total-IR luminosities have uncertainties of 50%. Since the derivations of both the 7.7 μm and total IR luminosity assume that starbursts dominate the infrared emission, the results for PAH-selected galaxies, the most plausible starburst candidates in our sample, should be the most reliable.

As shown in Fig. 10, some PAH-selected galaxies at $z \sim 1$ are ULIRGs. Their 7.7 μm peak luminosities are larger than local ULIRGs with a similar luminosity, and consistent with the PAH-to-total IR luminosity ratio of less luminous starbursts. They have no local counterparts and we specifically call these PAH-selected ULIRGs "PAH-luminous galaxies". The total IR luminosity of individual galaxies can be found in the legend of Figs. A.1−A.4. In our sample, we find no PAH-luminous galaxies at $z \sim 0.5$.

Normal starbursts, which have unabsorbed PAH emission features and no AGN contribution, can reach higher luminosity

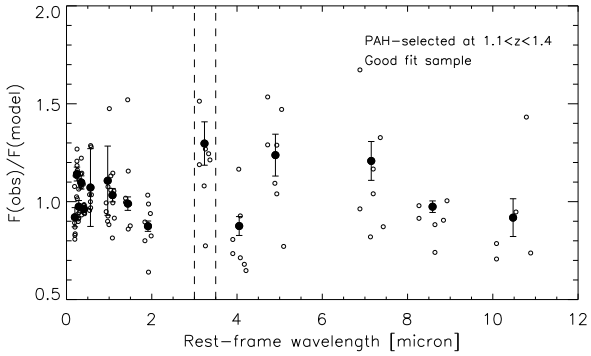

Fig. 11. Same as Fig. 9 but for PAH-selected galaxies at $1.1 < z < 1.4$. Open and solid circles indicate individual galaxies and the average for each photometric band, assuming a mean redshift of 1.22. Dashed lines bracket the 3.3 μm region.

at higher redshifts. Weedman & Houck (2008) reach the same conclusion by compiling various *Spitzer* IRS spectroscopic samples. Rigby et al. (2008) investigate the rest-frame 8 μm luminosity of galaxies at $z \sim 2$ as a function of total IR luminosity and find a similar trend. Using *Spitzer*/IRS, Huang et al. (2009) also report ULIRGs with high PAH-to-total IR luminosity ratio at $z \sim 2$. Our results show that there are extreme starbursts with ULIRG luminosity even at $z \sim 1$.

5.3. Photometric detection of PAH 3.3 μm feature?

For galaxies at $z \sim 1$, the PAH 3.3 μm feature falls into the $S7$ band. PAH-selected galaxies at $z \sim 1$ are good candidates for detecting this feature, because of both redshift and PAH prominence. Magnelli et al. (2008) made a similar attempt using *Spitzer* IRAC photometry for galaxies at $0.6 < z < 0.9$, and detected an excess over the stellar continuum, which may originate from the PAH 3.3 μm feature.

In Fig. A.3, we can see that some objects, i.e. ID2711, 2836, 2932, 3033, and 4956 have blue $S7 - S9W$ colours, which might be caused by the PAH 3.3 μm feature. Surprisingly, this excess is notable even if compared with the model flux that already includes the contribution from the 3.3 μm feature. We show the comparison of observed fluxes to model fluxes in Fig. 11. Here we use the sample of PAH-selected galaxies at $1.1 < z < 1.4$ with good SED fits. The average observed-to-model flux ratios range from 0.75 to 1.23, depending on the wavelength. At PAH-dominated wavelengths, i.e. >7 μm, the scatter is large and the ratios are marginally consistent with the model. At the rest-frame 3 μm band, including PAH 3.3 μm feature, the flux ratio is systematically high by a factor of 1.23 on average. If this excess is accounted for only by a systematically strong 3.3 μm feature, this feature must be unusually strong by a factor of 3–7, compared with the model. In the literature, no galaxies with such a strong 3.3 μm feature can be found to our knowledge. This anomaly could come from the continuum emission, rather than PAH 3.3 μm feature. However, we stress that, for galaxies at $z \sim 0.5$, the SBURT model reproduces the rest-frame 1–3 μm continuum emission well, as shown in Fig. 9.

It may be possible that the model lacks additional very hot dust components that contribute to the rest frame 3–4 μm emission. Such a near-IR excess with a colour temperature of $\sim 10^3$ K is reported in study of nearby galaxies (e.g. Lu et al. 2003; Flagey et al. 2006). However, we note that galaxies with large 3 μm flux tend to have small 4 μm flux as well, compared with the model. If the additional component has a grey body emission, it is difficult to explain such a trend. Furthermore, PAH-selected galaxies at $z \sim 0.5$ show no systematic near-IR excess, compared to the model, as shown in Fig. 9.

We need more careful investigation of the origin of the flux anomaly at this wavelength range. In fact, the model does not take into account the absorption features due to hydrogenated amorphous carbon (HAC) and/or H_2O. Unfortunately, we have to wait for the launch of JWST (Clampin 2008) and SPICA (Nakagawa 2004) to obtain mid-IR spectra of these galaxies and reveal the origin of this flux anomaly.

6. Summary

Using a multi-wavelength mid-IR survey, the AKARI NEP-deep, we have constructed a catalogue of all-band-detected sources. From this catalogue, we photometrically identified galaxies whose mid-IR emission is dominated by PAH emission. These PAH-selected galaxies have high PAH-to-continuum flux ratios, i.e. 11-to-7 μm and 15-to-9 μm flux ratios at $z \sim 0.5$ and 1, respectively. PAH-selected galaxies are the best candidates for starburst galaxies at these redshifts. Some of PAH-selected galaxies have stellar masses of $>3 \times 10^{10}\,M_\odot$ and could be progenitors of present-day massive galaxies, which are mostly spheroids.

An evolutionary SED model of starbursts, SBURT, reproduces observed optical-to-mid-IR SEDs of more than half of PAH-selected galaxies. According to the SED model, the PAH-to-continuum flux ratio of >8 can be explained with the starburst age of 0.4 Gyr or younger. The average starburst age from the SED fitting is 0.4 Gyr, which is marginally consistent with the PAH-to-continuum flux ratio. The lack of young starbursts may be the selection effect of the short lifetime of young starbursts. On the other hand, SBURT has a difficulty in reproducing the large PAH fluxes of optically red PAH-selected galaxies, which are probably evolved starbursts. This may require the SED model to include the age-dependent extinction and/or to adopt improved optical properties of PAHs.

At $z \sim 1$, the infrared luminosity of some PAH-selected galaxies corresponds to that of ULIRGs, and we call them PAH-luminous galaxies. They have high PAH luminosity, compared with local ULIRGs, but the PAH-to-total IR luminosity ratio is comparable to that of less luminous starbursts. PAH-luminous galaxies seem to be a unique galaxy population at high redshifts. The number density of PAH-luminous galaxies will be given elsewhere, using the whole area of the NEP-deep survey.

There is a hint that the PAH 3.3 μm feature is quite strong in PAH-luminous galaxies by a factor of 3–7, but this needs to be confirmed with next-generation infrared telescopes, such as JWST and SPICA, with infrared spectroscopy.

Acknowledgements. We would like to thank all the AKARI team members for their extensive efforts. We also appreciate the careful reading and constructive comments of the anonymous referee. This work is supported by the Japan Society for the Promotion of Science (JSPS; grant number 18·7747). This research is based on observations with AKARI, a JAXA project with the participation of ESA, and is partly supported with the Grant-in-Aid for Scientific Reserch (21340042) from the JSPS.

Appendix A: SED fitting results

Here we show the results of the SED fitting analysis of PAH-selected galaxies in Figs. A.1–A.4, and present the AKARI photometry in Table A.1. One source (ID4475) has problematic photometry in the S-cam images, owing to a nearby bright source, so is not included in the figure.

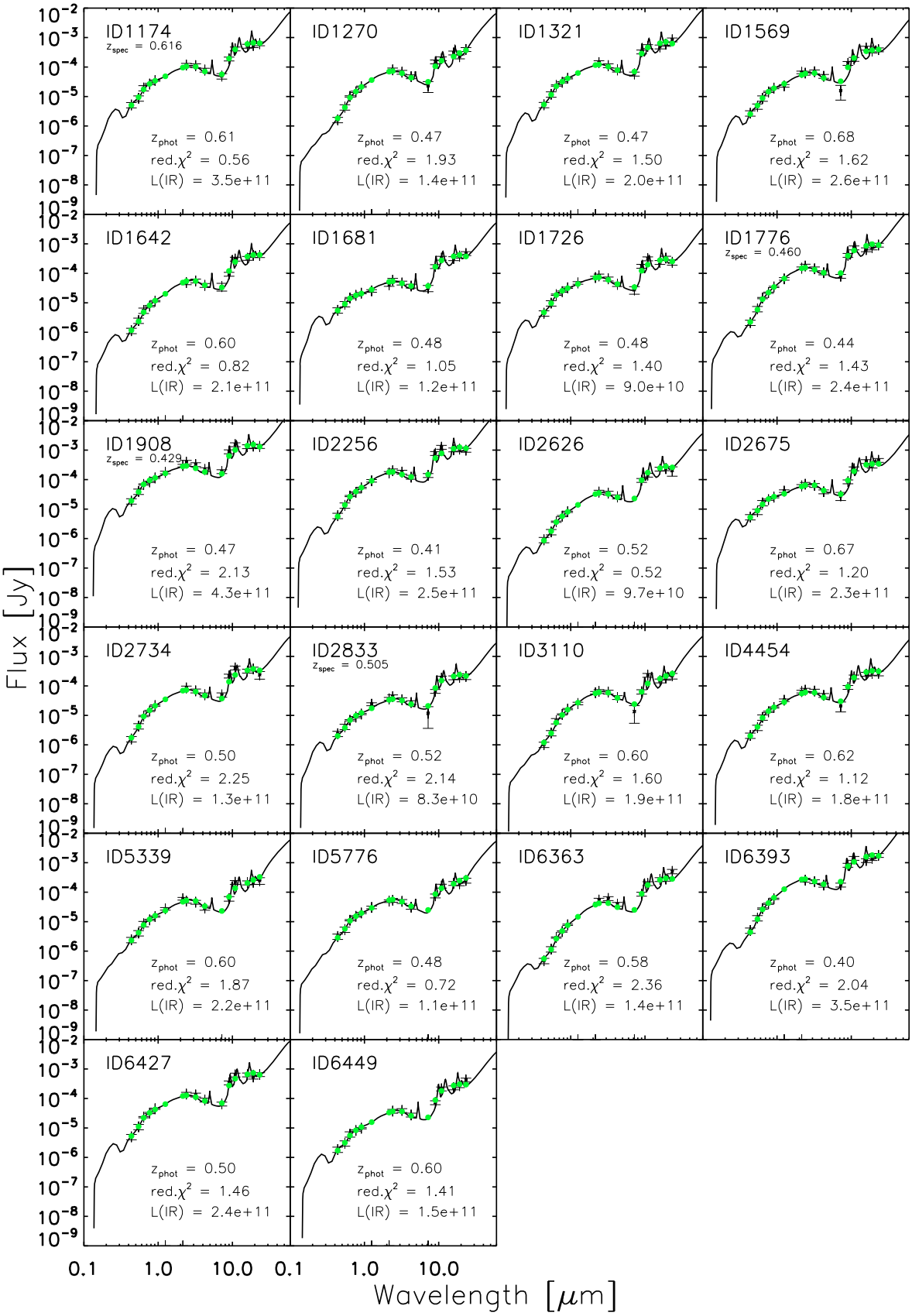

Fig. A.1. Results of SED fitting for PAH-selected galaxies at $z \sim 0.5$. Here we only show the good-fit sample. Data with error bars indicate the observed flux densities and errors adopted for the SED fitting. Solid circles are filter convolved fluxes of the best-fit model. Spectroscopic redshifts are reported if available.

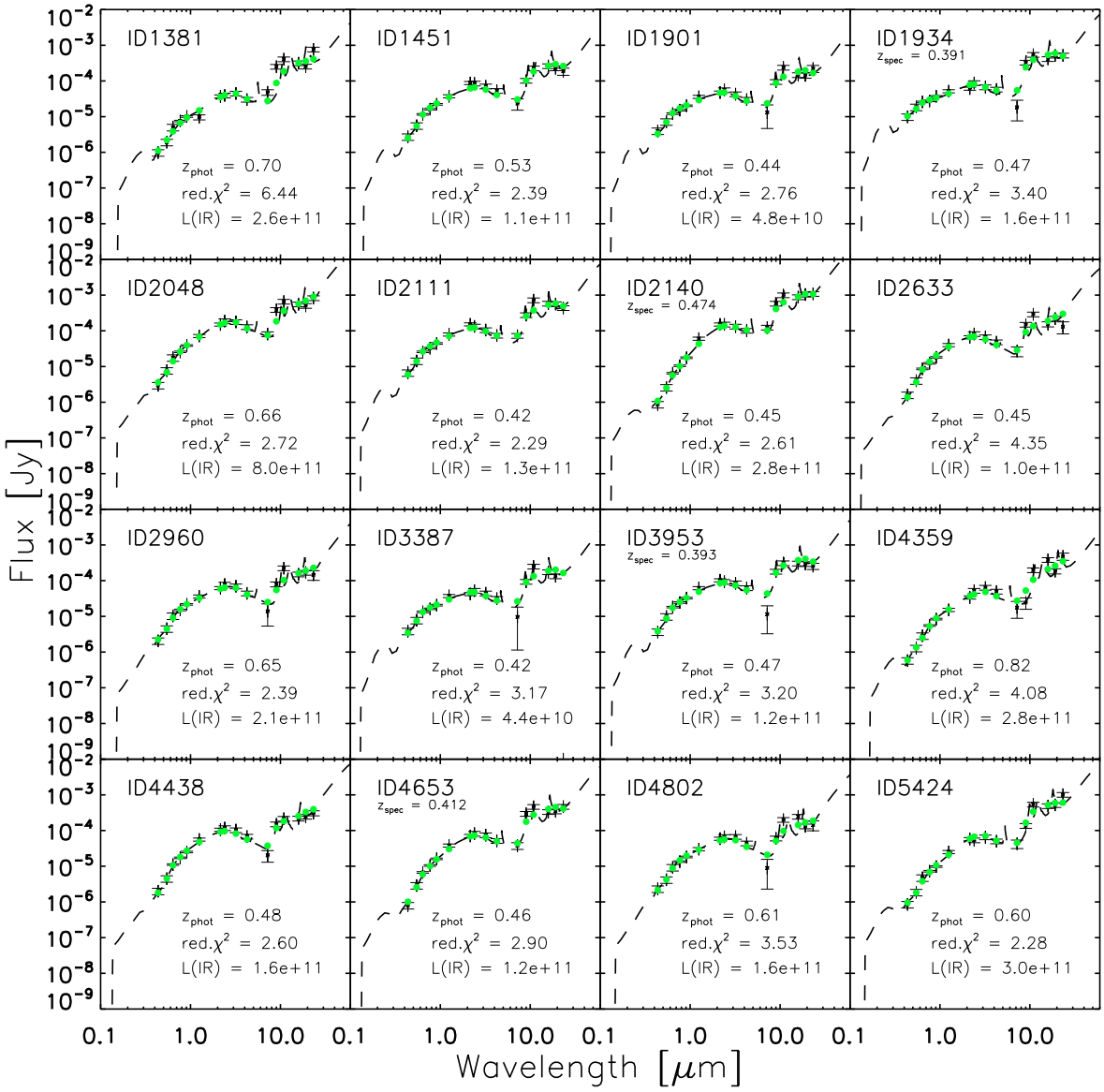

Fig. A.2. Same as Fig. A.1, but for the bad-fit sample.

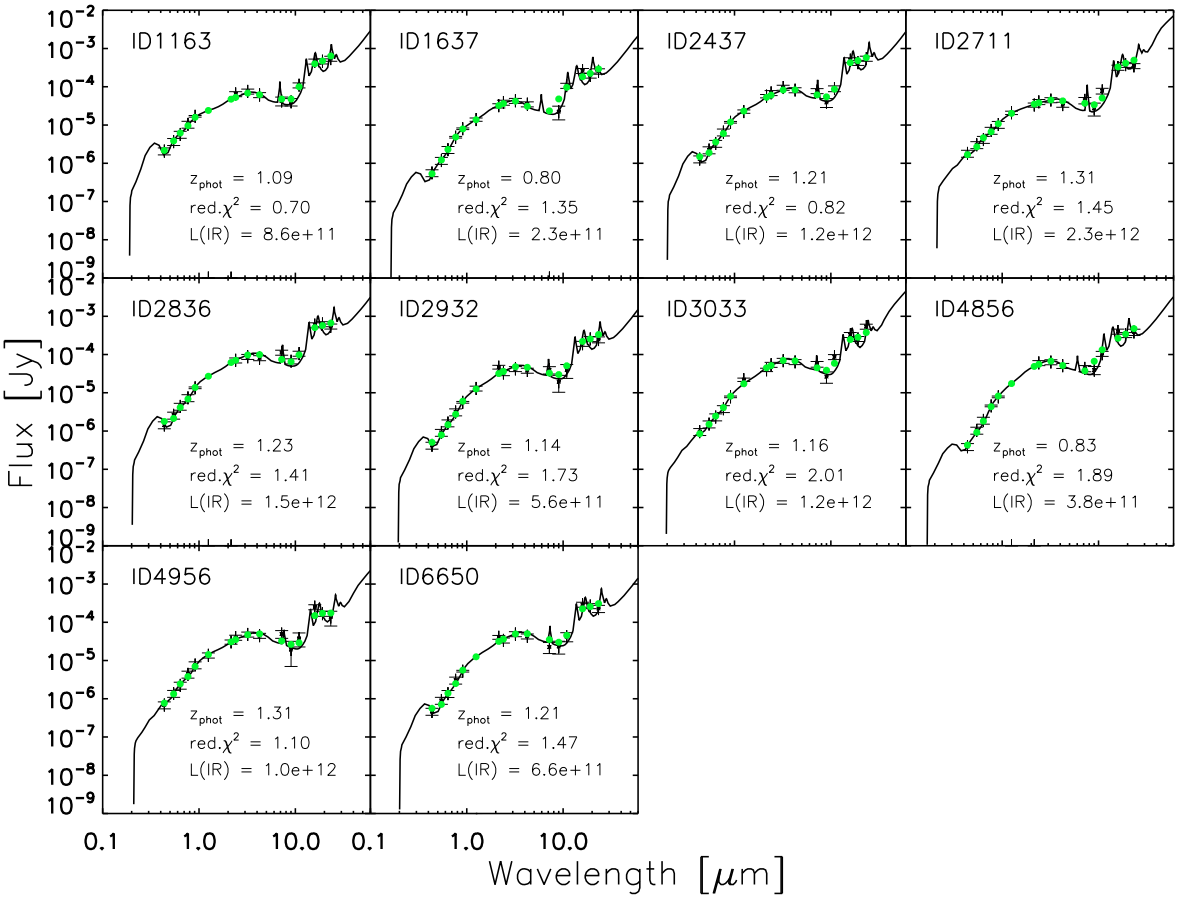

Fig. A.3. Same as Fig. A.1, but for PAH-selected galaxies at $z \sim 1$ with acceptable fits.

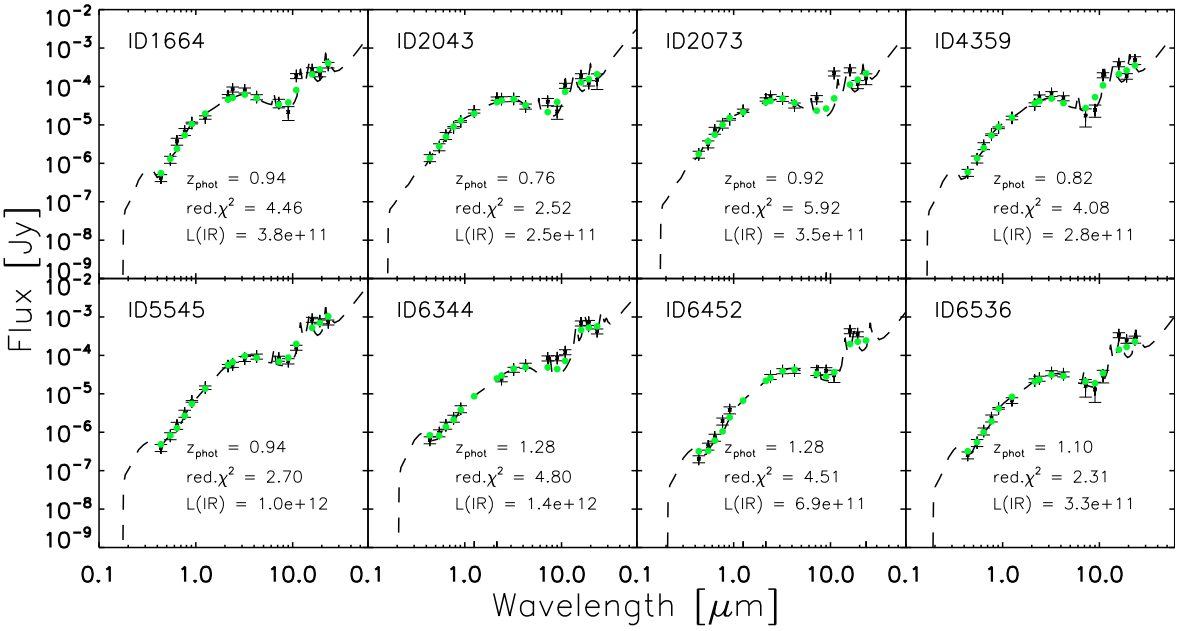

Fig. A.4. Same as Fig. A.3, but for the bad-fit sample.

Table A.1. AKARI coordinates and flux densities of PAH-selexted galaxies in the S-cam field.

ID	Name	RA	Dec	2.4 μm		3.2 μm		4.1 μm		7.0 μm		9.0 μm		11 μm		15 μm		18 μm		24 μm	
		[J2000]		f_ν	Δf_ν	f_ν	Δf_ν	f_ν	Δf_ν	f_ν	Δf_ν	f_ν	Δf_ν	f_ν	Δf_ν	f_ν	Δf_ν	f_ν	Δf_ν	f_ν	Δf_ν
				μJy	μJy	μJy	μJy	μJy	μJy	μJy	μJy	μJy	μJy	μJy	μJy	μJy	μJy	μJy	μJy	μJy	μJy
(1)	(2)	(3)	(4)	(5)	(6)	(7)	(8)	(9)	(10)	(11)	(12)	(13)	(14)	(15)	(16)	(17)	(18)	(19)	(20)	(21)	(22)
PAH-selected galaxies at $z \sim 1$																					
1163	J175331.44+662050.3	268.38102	66.34731	64.8	2.2	75.7	2.0	61.1	1.7	42.6	11.1	40.3	8.9	110.0	13.9	461.0	24.0	466.0	22.1	545.0	51.4
1637	J175611.19+662419.4	269.04663	66.40540	38.8	2.2	43.1	1.8	35.1	1.5	3.6	6.5	22.4	8.8	107.0	14.3	262.0	18.7	198.0	18.8	254.0	41.2
1664	J175342.76+662421.9	268.42817	66.40611	84.0	3.9	79.3	2.5	53.0	1.7	37.0	9.2	21.4	8.4	188.0	13.2	268.0	23.1	210.0	21.8	363.0	59.8
2043	J175323.76+662623.2	268.34902	66.43978	47.0	2.8	47.3	2.3	30.3	1.6	40.1	8.6	22.2	8.3	105.0	12.8	187.0	20.0	122.0	19.4	148.0	64.7
2073	J175636.92+662653.6	269.15387	66.44824	53.3	2.3	47.9	2.2	32.2	1.9	48.8	8.9	9.9	12.9	220.0	20.4	266.0	25.0	115.0	27.5	162.0	50.6
2437	J175322.46+662905.7	268.34360	66.48493	69.3	3.7	95.4	3.2	82.0	2.2	77.9	10.7	38.9	10.2	90.0	15.6	499.0	25.2	426.0	22.6	547.0	61.0
2711	J175346.89+663038.2	268.44540	66.51062	40.3	1.9	45.0	1.6	34.2	1.3	44.1	8.5	27.3	10.1	77.9	13.3	318.0	23.4	378.0	22.4	351.0	50.4
2836	J175726.41+663114.3	269.36005	66.52066	70.8	2.5	87.4	2.3	80.9	2.0	113.0	8.7	67.0	10.2	106.0	14.2	588.0	32.3	627.0	30.6	545.0	72.8
2932	J175336.29+663153.2	268.40124	66.53146	33.0	1.8	42.1	1.8	38.2	1.4	39.6	8.7	19.4	9.1	39.2	15.5	192.0	20.2	256.0	17.6	246.0	43.7
3033	J175458.78+663227.3	268.74493	66.54094	54.3	2.9	69.0	2.3	64.1	1.9	56.1	9.6	26.4	8.7	86.7	12.8	327.0	23.1	257.0	19.5	539.0	49.5
4359	J175629.33+664530.6	269.12221	66.75850	52.4	2.7	64.0	2.2	49.7	1.7	17.5	8.7	24.3	8.5	198.0	12.5	383.0	33.5	185.0	30.5	482.0	111.0
4856	J175731.87+664245.6	269.38281	66.71269	60.3	2.0	63.5	1.8	50.9	1.5	43.4	8.0	39.2	9.4	105.0	11.1	400.0	25.7	326.0	25.4	387.0	72.1
4956	J175412.75+664151.2	268.55316	66.69757	39.8	3.5	48.1	2.3	44.6	2.0	49.2	11.3	19.4	12.4	37.6	15.0	250.0	25.1	168.0	25.3	137.0	57.5
5545	J175328.41+663813.9	268.36838	66.63721	57.5	2.4	81.8	2.2	93.9	2.0	82.8	8.4	70.8	11.1	160.0	16.0	853.0	27.0	780.0	24.6	725.0	54.4
6344	J175416.38+665332.4	268.56829	66.89236	24.2	2.3	42.7	2.1	54.3	1.8	84.3	9.0	85.1	8.0	122.0	12.8	685.0	26.6	709.0	26.9	425.0	60.5
6452	J175732.98+665210.6	269.38742	66.86962	27.7	1.9	39.2	1.7	40.0	1.5	39.0	9.0	39.7	8.2	30.4	10.7	431.0	34.1	358.0	37.1	83.3	83.7
6536	J175456.40+665137.9	268.73504	66.86055	25.0	1.7	34.8	1.6	32.4	1.4	15.9	7.7	13.0	7.0	30.0	10.8	339.0	26.0	243.0	27.2	263.0	54.7
6650	J175433.94+665123.1	268.64142	66.85642	33.6	2.0	49.3	1.7	43.1	1.5	22.5	7.3	23.3	8.6	42.1	11.3	290.0	23.9	267.0	19.1	228.0	48.9
PAH-selected galaxies at $z \sim 0.5$																					
1174	J175731.27+662050.0	269.38033	66.34723	116.0	3.3	112.0	2.5	79.1	1.9	49.4	10.4	189.0	13.0	416.0	17.8	514.0	30.4	538.0	33.9	620.0	60.7
1270	J175526.98+662128.2	268.86244	66.35784	80.4	2.5	67.1	2.0	47.3	1.5	22.9	9.2	151.0	11.3	192.0	17.9	303.0	25.3	224.0	26.0	396.0	56.3
1321	J175700.71+662141.3	269.25297	66.36148	142.0	3.3	112.0	2.5	79.7	1.9	58.4	9.0	328.0	12.3	501.0	18.9	485.0	24.6	594.0	23.6	841.0	56.7
1381	J175650.63+662213.2	269.21097	66.37034	39.3	2.0	44.6	1.9	30.0	1.3	48.1	8.7	252.0	10.7	407.0	16.8	315.0	19.9	255.0	23.0	766.0	56.9
1451	J175559.22+662245.6	268.99678	66.37935	85.1	2.6	70.8	2.1	52.9	1.7	23.3	8.1	102.0	8.9	226.0	14.3	262.0	23.8	227.0	20.2	186.0	42.2
1569	J175600.05+662334.6	269.00021	66.39296	62.3	2.4	69.5	2.1	48.7	1.4	15.7	8.2	134.0	9.4	184.0	15.3	441.0	26.0	354.0	22.5	388.0	48.4
1642	J175345.99+662357.8	268.44166	66.39940	48.4	3.7	55.4	3.5	39.2	2.3	35.4	10.4	93.8	10.1	306.0	15.6	325.0	26.9	406.0	25.0	403.0	56.1
1681	J175640.43+662403.8	269.16847	66.40106	58.4	2.4	47.2	2.0	37.1	1.6	31.3	7.5	171.0	9.7	328.0	15.9	318.0	20.5	387.0	19.8	471.0	46.4
1726	J175629.54+662444.9	269.12310	66.41249	81.9	2.5	64.9	2.0	42.2	1.5	27.4	7.9	175.0	13.1	313.0	14.8	236.0	20.9	329.0	19.7	238.0	49.0
1776	J175631.43+662447.1	269.13098	66.41309	177.0	3.5	143.0	2.7	105.0	2.1	80.0	9.0	411.0	13.7	738.0	18.1	637.0	26.7	738.0	24.6	914.0	53.9
1901	J175630.45+662550.4	269.12690	66.43068	55.6	2.1	42.7	1.6	30.0	1.2	13.0	8.3	94.5	14.1	237.0	20.3	147.0	19.7	143.0	23.9	222.0	50.2
1908	J175518.76+662529.8	268.82820	66.42497	391.0	5.0	325.0	3.9	221.0	2.9	188.0	11.3	888.0	15.0	1540.0	21.9	1320.0	29.0	1370.0	26.3	1340.0	56.4
1934	J175427.51+662545.6	268.61465	66.42934	87.7	2.5	67.0	2.1	57.8	1.7	18.2	10.6	329.0	12.6	543.0	17.5	414.0	23.7	518.0	23.6	520.0	48.0
2048	J175415.43+662625.6	268.56430	66.44046	187.0	3.4	177.0	3.0	128.0	2.3	81.1	9.8	387.0	11.7	659.0	17.5	553.0	22.6	502.0	22.7	827.0	53.9
2111	J175537.50+662702.4	268.90628	66.45067	133.0	2.9	105.0	2.3	73.7	1.7	72.6	9.0	276.0	12.1	722.0	18.1	581.0	25.0	562.0	24.1	437.0	48.2
2140	J175641.58+662704.5	269.17325	66.45126	151.0	3.4	132.0	3.0	101.0	2.3	124.0	9.4	580.0	16.4	996.0	21.2	881.0	27.0	1040.0	27.0	1090.0	60.2
2256	J175652.48+662736.3	269.21869	66.46011	200.0	3.6	181.0	2.9	121.0	2.2	139.0	9.1	778.0	20.0	1260.0	22.4	1030.0	29.2	1080.0	26.1	998.0	56.8
2626	J175721.13+663009.3	269.33805	66.50260	37.8	1.8	35.0	1.4	26.2	1.2	2.3	6.7	94.8	10.9	143.0	14.7	229.0	27.7	236.0	29.4	201.0	70.6
2633	J175352.59+662951.3	268.46913	66.49761	81.7	2.4	66.6	1.9	48.0	1.5	27.1	8.3	149.0	10.0	290.0	17.3	154.0	25.4	220.0	22.8	130.0	48.0
2675	J175325.50+662957.2	268.35625	66.49923	69.9	2.2	63.7	1.8	38.9	1.3	28.1	8.6	85.0	8.4	235.0	13.7	414.0	25.1	291.0	22.5	453.0	53.9
2734	J175723.08+663038.5	269.34619	66.51071	85.7	2.6	68.1	2.1	50.1	1.7	49.6	8.4	218.0	12.9	409.0	15.8	321.0	27.6	376.0	29.4	238.0	69.1
2833	J175346.60+663101.8	268.44418	66.51717	43.2	2.0	34.0	1.6	27.3	1.4	11.7	8.1	65.8	8.7	184.0	15.4	190.0	22.1	196.0	20.8	210.0	45.9
2960	J175327.78+663138.8	268.36579	66.52745	78.2	2.5	69.8	2.0	44.3	1.5	13.9	8.5	79.4	12.1	224.0	16.0	151.0	21.6	168.0	21.0	146.0	44.1

Notes. Galaxies with ambiguous optical identification are excluded. Column (1): AKARI mid-IR source ID. Columns (2): Source Name. Columns (3) and (4): AKARI *N*2-band J2000.0 RA and Dec. Columns (5) through (22): IRC flux densities and errors.

Table A.1. continued.

ID	Name	RA	Dec	2.4 μm		3.2 μm		4.1 μm		7.0 μm		9.0 μm		11 μm		15 μm		18 μm		24 μm	
		[J2000]		f_ν μJy	Δf_ν μJy	f_ν μJy	Δf_ν μJy	f_ν μJy	Δf_ν μJy	f_ν μJy	Δf_ν μJy	f_ν μJy	Δf_ν μJy	f_ν μJy	Δf_ν μJy	f_ν μJy	Δf_ν μJy	f_ν μJy	Δf_ν μJy	f_ν μJy	Δf_ν μJy
(1)	(2)	(3)	(4)	(5)	(6)	(7)	(8)	(9)	(10)	(11)	(12)	(13)	(14)	(15)	(16)	(17)	(18)	(19)	(20)	(21)	(22)
3110	J175331.90+663231.9	268.38295	66.54220	65.1	2.3	61.9	1.9	40.7	1.5	13.4	8.0	63.3	10.7	230.0	19.0	149.0	20.4	184.0	22.8	218.0	46.7
3387	J175345.13+663405.1	268.43805	66.56809	52.5	2.5	44.4	2.2	31.3	1.7	9.7	8.5	93.6	11.8	250.0	19.4	174.0	24.0	134.0	20.3	33.7	45.4
3953	J175456.90+664818.7	268.73711	66.80520	93.2	2.7	84.9	2.3	62.1	1.8	11.5	8.2	180.0	10.4	311.0	14.1	305.0	27.3	294.0	21.9	256.0	50.3
4359	J175629.33+664530.6	269.12221	66.75850	52.4	2.7	64.0	2.2	49.7	1.7	17.5	8.7	24.3	8.5	198.0	12.5	383.0	33.5	185.0	30.5	482.0	111.0
4438	J175319.00+664419.7	268.32918	66.73881	118.0	2.9	103.0	2.3	68.0	1.7	20.2	7.2	150.0	10.3	215.0	13.4	218.0	20.9	245.0	19.1	308.0	49.1
4454	J175335.34+664522.4	268.39727	66.75624	72.0	2.7	67.1	2.1	47.9	1.7	20.8	7.7	89.8	11.1	203.0	14.0	251.0	21.9	270.0	19.2	268.0	48.1
4653	J175645.64+664334.9	269.19020	66.72637	82.1	3.2	74.2	2.4	51.6	2.2	37.6	8.1	296.0	10.1	463.0	12.9	333.0	27.8	347.0	23.3	465.0	64.4
4802	J175328.00+664228.0	268.36667	66.70779	66.5	2.3	67.2	2.2	43.9	2.0	8.9	6.6	60.5	9.2	200.0	11.2	245.0	19.8	132.0	17.7	143.0	44.7
5339	J175651.89+664003.0	269.21623	66.66751	50.0	2.4	45.8	2.2	28.8	2.1	7.8	9.7	60.2	10.5	217.0	13.2	209.0	32.0	216.0	29.5	247.0	62.9
5424	J175534.22+663918.4	268.89262	66.65512	53.7	2.0	65.1	1.9	50.2	1.4	42.7	11.4	136.0	12.7	538.0	19.1	487.0	35.9	522.0	47.6	1010.0	96.6
5776	J175328.61+663701.4	268.36922	66.61707	53.6	2.0	48.8	1.8	31.0	1.4	3.2	7.0	75.2	10.8	162.0	16.3	200.0	19.8	195.0	18.2	250.0	47.6
6363	J175701.56+665331.4	269.25654	66.89206	54.1	2.4	61.1	2.3	39.0	1.7	4.4	7.4	86.4	9.8	197.0	13.2	270.0	25.6	278.0	30.6	507.0	86.5
6393	J175402.88+665222.2	268.51203	66.87284	257.0	4.5	229.0	3.3	174.0	2.8	176.0	10.2	828.0	11.9	1420.0	17.9	1190.0	29.8	1400.0	28.7	1780.0	62.0
6427	J175430.88+665249.1	268.62869	66.88033	141.0	3.1	132.0	2.7	89.1	2.1	65.5	7.9	342.0	9.4	630.0	14.9	636.0	26.4	537.0	22.1	653.0	50.6
6449	J175542.96+665248.9	268.92901	66.88027	37.2	1.9	39.3	1.7	27.6	1.4	7.5	7.8	72.5	8.4	213.0	12.5	232.0	28.0	274.0	23.5	426.0	57.9

Notes. Column (1): AKARI mid-IR source ID. Columns (2): Source name. Columns (3) and (4): AKARI *N*2-band J2000.0 RA and Dec. Columns (5) through (22): IRC flux densities and errors.

References

Babbedge, T. S. R., Rowan-Robinson, M., Vaccari, M., et al. 2006, MNRAS, 370, 1159

Bertin, E., & Arnouts, S. 1996, A&AS, 117, 393

Blain, A. W., Chapman, S. C., Smail, I., & Ivison, R. 2004, ApJ, 611, 725

Bolzonella, M., Miralles, J.-M., & Pelló, R. 2000, A&A, 363, 476

Borys, C., Smail, I., Chapman, S. C., et al. 2005, ApJ, 635, 853

Bouché, N., Cresci, G., Davies, R., et al. 2007, ApJ, 671, 303

Brandl, B. R., Bernard-Salas, J., Spoon, H. W. W., et al. 2006, ApJ, 653, 1129

Bruzual, G., & Charlot, S. 2003, MNRAS, 344, 1000

Calzetti, D., Armus, L., Bohlin, R. C., et al. 2000, ApJ, 533, 682

Caputi, K. I., Lagache, G., Yan, L., et al. 2007, ApJ, 660, 97

Chapman, S. C., Blain, A. W., Smail, I., & Ivison, R. J. 2005, ApJ, 622, 772

Cimatti, A., Daddi, E., & Renzini, A. 2006, A&A, 453, L29

Clampin, M. 2008, Adv. Space Res., 41, 1983

Elbaz, D., Daddi, E., Le Borgne, D., et al. 2007, A&A, 468, 33

Farrah, D., Bernard-Salas, J., Spoon, H. W. W., et al. 2007, ApJ, 667, 149

Farrah, D., Lonsdale, C. J., Weedman, D. W., et al. 2008, ApJ, 677, 957

Flagey, N., Boulanger, F., Verstraete, L., et al. 2006, A&A, 453, 969

Genzel, R., Lutz, D., Sturm, E., et al. 1998, ApJ, 498, 579

Goto, T., Takagi, T., Matsuhara, H., et al. 2010, 514, A6

Heavens, A., Panter, B., Jimenez, R., & Dunlop, J. 2004, Nature, 428, 625

Houck, J. R., Weedman, D. W., Le Floc'h, E., & Hao, L. 2007, ApJ, 671, 323

Huang, J.-S., Faber, S. M., Daddi, E., et al. 2009, ApJ, 700, 183

Hunt, L. K., Malkan, M. A., Salvati, M., et al. 1997, ApJS, 108, 229

Imai, K., Matsuhara, H., Oyabu, S., et al. 2007, AJ, 133, 2418

Imanishi, M., Dudley, C. C., Maiolino, R., et al. 2007, ApJS, 171, 72

Kodama, T., & Arimoto, N. 1997, A&A, 320, 41

Le Floc'h, E., Papovich, C., Dole, H., et al. 2005, ApJ, 632, 169

Li, A., & Draine, B. T. 2001, ApJ, 554, 778

Lu, N., Helou, G., Werner, M. W., et al. 2003, ApJ, 588, 199

Lutz, D., Spoon, H. W. W., Rigopoulou, D., Moorwood, A. F. M., & Genzel, R. 1998, ApJ, 505, L103

Magnelli, B., Chary, R. R., Pope, A., et al. 2008, ApJ, 681, 258

Melbourne, J., Ammons, M., Wright, S. A., et al. 2008, AJ, 135, 1207

Nakagawa, T. 2004, Adv. Space Res., 34, 645

Nardini, E., Risaliti, G., Salvati, M., et al. 2008, MNRAS, 385, L130

Pérez-González, P. G., Rieke, G. H., Egami, E., et al. 2005, ApJ, 630, 82

Polletta, M., Tajer, M., Maraschi, L., et al. 2007, ApJ, 663, 81

Pope, A., Chary, R.-R., Alexander, D. M., et al. 2008, ApJ, 675, 1171

Rigby, J. R., Marcillac, D., Egami, E., et al. 2008, ApJ, 675, 262

Rigopoulou, D., Spoon, H. W. W., Genzel, R., et al. 1999, AJ, 118, 2625

Smail, I., Chapman, S. C., Blain, A. W., & Ivison, R. J. 2004, ApJ, 616, 71

Tacconi, L. J., Genzel, R., Smail, I., et al. 2008, ApJ, 680, 246

Takagi, T., Arimoto, N., & Vansevičius, V. 1999, ApJ, 523, 107

Takagi, T., Arimoto, N., & Hanami, H. 2003a, MNRAS, 340, 813

Takagi, T., Vansevicius, V., & Arimoto, N. 2003b, PASJ, 55, 385

Takagi, T., Hanami, H., & Arimoto, N. 2004, MNRAS, 355, 424

Takagi, T., Matsuhara, H., Wada, T., et al. 2007a, PASJ, 59, 557

Takagi, T., Mortier, A. M. J., Shimasaku, K., et al. 2007b, MNRAS, 381, 1154

Tanabé, T., Sakon, I., Cohen, M., et al. 2008, PASJ, 60, 375

Valiante, E., Lutz, D., Sturm, E., et al. 2007, ApJ, 660, 1060

Wada, T., Matsuhara, H., Oyabu, S., et al. 2008, PASJ, 60, 517

Wang, Z., Fazio, G. G., Ashby, M. L. N., et al. 2004, ApJS, 154, 193

Weedman, D. W., & Houck, J. R. 2008, ApJ, 686, 127

Weedman, D. W., Hao, L., Higdon, S. J. U., et al. 2005, ApJ, 633, 706